Nickel Phosphides Fabricated through a Codeposition−Annealing Technique as Low-Cost Electrocatalytic Layers for Efficient Hydrogen Evolution Reaction

R. Bernasconi, M. I. Khalil, C. Iaquinta, C. Lenardi, L. Nobili, and L. Magagnin*

Cite This: *ACS Appl. Energy Mater.* 2020, 3, 6525−6535

Read Online

ACCESS | 📊 Metrics & More | 📰 Article Recommendations | 🆂🅸 Supporting Information

ABSTRACT: Water splitting will be one of the most strategic techniques in the upcoming hydrogen-based economy. In this context, the development of efficient and low-cost Pt-free electrocatalysts is crucial to make it economically viable. The present work proposes a low-cost and scalable methodology to produce electrocatalytic layers based on nickel phosphide for hydrogen evolution reaction. In particular, a nickel−phosphorus solid solution is electrolytically codeposited together with red phosphorus particles. This approach overcomes the compositional limit typical of electrodeposited Ni−P by providing a supplementary phosphorous source directly embedded in the layer and makes it possible to synthesize high-P phosphides such as $Ni_{12}P_5$ and Ni_2P. The obtained composites are subjected to different annealing cycles to precipitate phosphides, evidencing a major influence of process conditions on the final phase composition. X-ray photoelectron spectroscopy reveals the presence of a phosphorus-depleted region in correspondence of the surface of the samples. Finally, layers are tested to assess their electrocatalytic performances, and the effects of annealing time and catalyst loading are investigated. Samples with an optimized content of Ni_2P evidence the lowest overpotential values, with 224 mV at 10 mA/cm^2, and good stability over time.

KEYWORDS: nickel phosphide, red phosphorus, codeposition, electrocatalysis, hydrogen evolution reaction
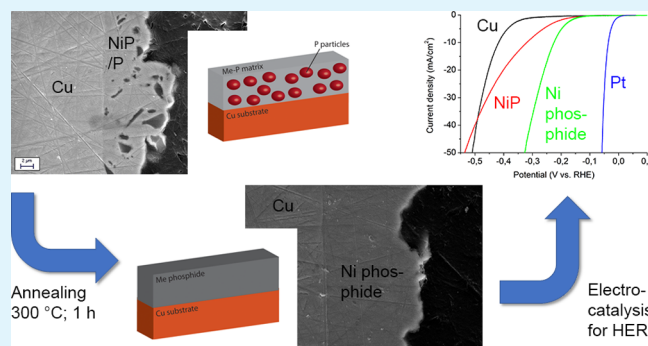
1. INTRODUCTION

The modern world is dominated by a constantly increasing need of sustainable and renewable energy production technologies.[1] In this context, many critical topics in modern research are strictly connected to energy. The most critical part of the sustainable energy supply chain is the production step, which must be necessarily based on carbon-free sources. However, also storage strategies play a fundamental role for an efficient energy supply strategy, especially in the case of intermittent energy sources such as solar or wind.[2] Consequently, electrochemistry is at the forefront in research on energy, with the development of highly efficient batteries, accumulators, and storage technologies.[3] Between long-term storage techniques, hydrogen is probably one of the most promising. The great interest in hydrogen handling arises from the possibility, widely demonstrated, of using fuel cells as devices for sustainable energy conversion.[4,5] Moreover, hydrogen will be fundamental, in perspective, for usage in nuclear fusion power plants[6] currently under development. Hydrogen is highly advantageous as energy storage medium because it can be obtained easily from water and the final product of its oxidation is again water. The absence of dangerous emissions, such as CO_2, and the good energy density per unit mass[7] make hydrogen very attractive for technological applications.

As already outlined, hydrogen can be obtained from water via electrolysis.[8] During this process water splits, hydrogen evolution reaction (HER) takes place at the cathode and oxygen evolution reaction (OER) at the anode. In normal conditions, HER requires an electrochemical overpotential to happen on the electrode surface.[9] For this reason, electrocatalysts are routinely employed to lower the energy barrier required for molecular hydrogen generation. HER on an electrocatalyst requires considerably lower overpotentials with respect to nonelectrocatalytic surfaces.[10−12] In general, noble metals are classical catalysts for HER, yielding optimal overpotentials.[12] These materials are however also costly and rare, and these exact reasons induced researchers to investigate
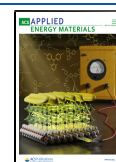
possible low-cost alternatives for both HER and OER.[13−15] Consequently, a wealth of electrocatalytic materials have been developed in the last few decades. Notable examples range from metals/alloys[16,17] and their nanoparticles (NPs)[18] to metal sulfides,[19] selenides,[20,21] phosphides,[22−25] nitrides,[20,26] or carbides.[20,26]

The electrocatalytic material considered in the present work is nickel phosphide, one of the most promising candidates to substitute Pt-based catalysts. In general, all the existing compounds of Ni and P present some degree of electro-catalytic activity,[22,27,28] which depends in particular on the phosphorus content.[29,30] Nickel phosphides, the Ni_2P compound in particular, are characterized by low HER overpotential and long-term stability when in a thin film, nanostructured or not, or NP form.[31] As an example, Read et al.[32] reported an overpotential of 128 mV at 10 mA/cm² in the case of Ni_2P supported on Ni and obtained reacting organophosphines with commercial Ni foil. The peculiar synthesis route followed by Read et al. offers the opportunity to discuss Ni_2P fabrication, which is not trivial. The production of the pure Ni_2P phase, with no secondary compounds, requires strictly controlled synthesis routes. The material, especially in the form of NPs or nanowires, can be obtained by the decomposition of metal-phosphine moieties,[31] by hydro-thermal synthesis[33−35] or by direct phosphorization of Ni.[36−38] Conversely, thin films and nanofoams can be prepared by direct phosphorization of Ni films obtained by electro-deposition or sputtering.[39,40] It should be emphasized that most thin film manufacturing methodologies involve the presence of poisonous P compounds, such as phosphine[41] or elemental phosphorus at high temperatures. Both are danger-ous, but the latter is particularly unsafe because of the possible formation of the white P allotrope, which is explosive and poisonous,[42] from P vapors condensing in cold zones of synthesis equipment.[43] Moreover, methods such as direct phosphorization are relatively laborious and do not optimize P usage, resulting in considerable material waste. It is therefore of interest the development of a low-cost direct phosphorization methodology that reduces elemental P usage and provides a good control over final electrocatalyst stoichiometry.

Starting from these premises, we developed a novel and highly scalable manufacturing strategy for electrocatalytic Ni_2P. As the first step, we electrochemically codeposited a metastable Ni−P solid solution matrix together with elemental phospho-rus particles.[44−46] An annealing step was then performed to favor P interdiffusion in the Ni−P matrix and formation of phosphide phases. A similar approach has been employed in the past for the fabrication of corrosion-resistant copper−phosphorus alloys.[47] In the process described in the present work, the necessity of codepositing Ni−P with P arises from the fact that the electrochemical deposition of Ni−P alone from modified Watts electrolytes is not capable of yielding the correct stoichiometry for Ni_2P (33% at. P) because of the compositional limit (25% at.) in P content typical of electrolytic deposition.[44,45] A possible way to overcome this limit is the codeposition of elemental P particles with Ni−P. It must be emphasized that, by doing this, the source of P for phosphorization is directly embedded in the deposited layer, with no need of a P containing atmosphere. Both P contained in the Ni−P solid solution and elemental red P contribute to the formation of Ni_2P. Because elemental P is confined inside the coating, negligible P outgassing in the external atmosphere is allowed and white P formation is avoided. Additionally, an optimal P usage can be guaranteed by applying the approach described here, which allows fast and easy electrocatalytic layer production on a variety of substrates.

2. EXPERIMENTAL SECTION

2.1. Electrocatalytic Layer Synthesis. All the chemicals employed were acquired from Sigma-Aldrich and used as received. A base deposition bath for Ni−P contained 180 g L⁻¹ of $NiSO_4$·$6H_2O$, 24 g L⁻¹ of $NiCl_2$·$6H_2O$, 30 g L⁻¹ of H_3PO_4, and 20 g of L⁻¹ H_3PO_3. pH of the electrolyte was corrected to 2 using NaOH. Before performing Ni−P/P codeposition, red P particles were added to the bath, which was then subjected to a sedimentation process to remove larger P particles. The details of such a sedimentation process, which resemble similar processes reported in the literature,[48] are as follow: an excess of 40 g of red phosphorous was dispersed in 200 mL of Ni−P electrolyte using sonication in order to break particles aggregates. A 250 mL beaker was employed to contain the resulting 200 g L⁻¹ suspension. After 50 s, the upper part of the liquid was removed and the solid precipitated on the bottom was discarded. The final suspension of P in the Ni−P electrolyte thus obtained, which was characterized by a P content much lower than the initial 200 g L⁻¹, was sonicated again to disperse P particles and kept under stirring before deposition. Ni−P/P deposition was performed at 20 mA cm⁻², 50 °C, and vigorous stirring. Deposition time was fixed at 90 min, except for the test carried out to evaluate the effect of catalyst loading. Copper plates were employed as substrates. Before deposition, their surface was cleaned with acetone and deoxidized with a 6.5% HNO_3 solution (5 s immersion time). After the deposition step, the samples were washed thoroughly with demineralized water to eliminate residual P particles from the surface and carefully dried with N_2. Annealing was performed in a tubular oven, in the presence of a N_2 protective atmosphere. Annealing time and temperature were varied as described in the text.

2.2. Electrocatalytic Layer Characterization. Scanning elec-tron microscopy (SEM) characterization was performed by mean of a Zeiss EVO 50 electron microscope, equipped with an Oxford Instruments model 7060 EDS module. The samples were observed directly on their surface and also on their cross sections. To prepare the latter, samples were cut, incorporated in the epoxy resin and polished to a mirror-like finish. The instrument employed to perform transmission electron microscopy (TEM) analysis was a Philips CM 200. X-ray diffraction (XRD) spectra were acquired using a Philips PW 1830 diffractometer in thin film configuration with Cu Kα radiation (λ = 1.5406 Å). The XPS measurements were carried out with a PHI 5600 UHV apparatus equipped with a hemispherical electron analyzer and a monochromatized X-ray source (Al Kα = 1486.6 eV, ΔE = 0.48 eV). The high-resolution spectra were acquired in constant step energy mode with E_{pass} = 23.8 eV. The overall energy resolution was 0.8 eV. The pressure in the experimental chamber during experiments was 1.2 × 10⁻⁹ mbar. The binding energy scale was calibrated via the Au $4f_{7/2}$ core level line (located at 84.00 eV) of a clean polycrystalline Au sample. To remove superficial contaminants and oxides the samples were sputtered at selected time intervals with a PHI 04-303 differential ion gun operating in rastering mode. The argon ion energy was set at 2 keV with ion current on a sample of 5 μA (pressure in the main chamber up to ∼1 × 10⁻⁸ mbar). Voigt line-shape and Shirley background were used to fit the peaks and the background, respectively. Least square curve-fitting was performed using the programs KolXPD and Igor Pro.

2.3. Electrochemical Characterization. Electrocatalysis tests were carried out using the active phosphide-containing material as the working electrode in an electrochemical cell comprising graphite as the counter electrode and a 3 M KCl Ag/AgCl standard electrode as the reference. A 0.5 M H_2SO_4 solution was used as the electrolyte. Tests were performed at ambient temperature and under vigorous stirring. Potential was varied at 2 mV/s in all the tests except the multicycle analysis, where the scan rate was changed to 50 mV/s. No Ohmic correction was applied, but the reference electrode was kept as close as possible to the working electrode to limit potential drops. A
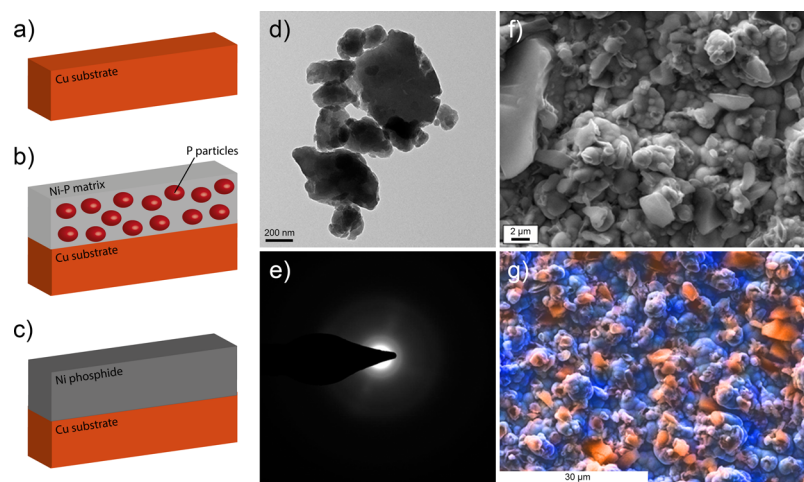
Figure 1. Electrocatalytic layer manufacturing process: Cu substrate (a), Ni−P/P codeposition (b), annealing to favor interdiffusion and phosphide precipitation (c); TEM image of P microparticles (d); SAED of P microparticles (e); SEM picture of the Ni−P/P codeposit before annealing (f); and false color elemental mapping for the Ni−P/P codeposit before annealing (g), P is highlighted in orange and Ni is highlighted in blue.

standard commercial 20% Pt catalyst was characterized together with the samples produced and used as a reference material to compare electrocatalytic properties. Each electrocatalysis test was performed on two samples and the best result is reported in the paper. In all cases, a deviation of more than 5.5% between the tests was never observed.

3. RESULTS AND DISCUSSION

3.1. Electrocatalytic Layer Manufacturing Process. A highly scalable and low-cost process, consisting of two distinct steps, was followed to obtain Ni_2P electrocatalytic layers. The first part of the method was based on the codeposition on a Cu substrate (Figure 1a) of a Ni−P matrix, which is a solid solution of the two elements, with microparticles of elemental red phosphorus (Figure 1b). In order to maximize the overall amount of phosphorus, it was convenient to deposit a high-P alloy as the matrix for the composite. For this reason, a modified Watt's bath able to yield 22.8% at. P was employed for the experimentation. Red P particles were uniformly dispersed in such an electrolyte, allowing them to be codeposited inside the matrix. Initially, as received particles were characterized and found to have mean diameters ranging between one hundred nanometer and some micrometers. After dispersion, the largest particles (more than 1−2 μm) were removed from the solution introducing a sedimentation step before codeposition. The procedure yielded a more uniform distribution of the particle diameters. Figure 1d depicts the TEM appearance of the particles employed. Their structure is amorphous, as evidenced by the selected area electron diffraction (SAED) pattern reported in Figure 1e.

The second step of the process was a controlled annealing treatment performed to promote interdiffusion and phosphide precipitation (Figure 1c). During this step, elemental phosphorus diffused inside the Ni−P matrix and reacted to form compounds with Ni. In addition, P dissolved in the solid solution reacted with Ni as well. The final desired result was a homogeneous layer containing only phosphides, whose relative percentage was tuned by modifying annealing parameters.

3.2. Ni−P/P Codeposition. In the first step of the manufacturing process, Ni−P was codeposited with red P microparticles suspended in the electrodeposition bath. To maximize P content, a high quantity of microparticles was added. The initial P concentration, equal to 200 g L^{-1},

decreased to roughly 70 g L^{-1} after the sedimentation process. The main visible effect of the codeposition was the significant increase in surface roughness. Figure S1 depicts the appearance of Ni−P deposited without P particles, while Figure 1f shows the appearance of layers containing the microparticles. The particle-free layer is characterized by a smooth surface, presenting a R_a roughness value of 154 ± 24 nm. Conversely, it is evident that the morphology is greatly altered by the codeposition with P. Figure 1f depicts an irregular and rough surface, on which the particles are clearly visible. From the quantitative point of view, roughness R_a increased to 683 ± 87 nm. The second visible effect of the codeposition is the notable increase in P content, which nearly doubled to 43% at. (from the 22.8% at. of the matrix without particles). To gather evidence for P particles distribution, SEM elemental mapping was performed on the surface of the codeposit before annealing. Figure 1g depicts the result obtained, with P highlighted in orange and Ni in blue. It is evident from the image that red P particles are reasonably well dispersed inside the matrix. Obtaining a good dispersion is useful for the subsequent interdiffusion step because homogeneously distributed particles imply that the thickness of the matrix between them is roughly constant. Thus, elemental P, which diffuses isotropically around the particles themselves, does not accumulate in some zones of the coating or becomes depleted in some others.

3.3. Ni−P/P Annealing. After codeposition, Ni−P/P layers were subjected to annealing at standard pressure in a N_2 protective atmosphere. Ni−P/P annealing is the most critical step of the process to obtain a pure Ni_2P phase. The nickel−phosphorus phase diagram is characterized by the presence of many compounds,[49] including Ni_3P, $Ni_{12}P_5$, Ni_2P, Ni_5P_4, NiP, and NiP_2. The final phase composition is therefore expected to depend on the parameters selected for the annealing treatment.

Figure 2a depicts the SEM appearance of a sample after 2 h annealing at 400 °C. Isolated P particles are no more present, as confirmed by elemental mapping. The overall morphology is similar to the nonannealed sample (Figure 1f), with the only exception being some fibrous bush-like structures that are clearly visible on the surface. When analyzed with EDS, such structures do not evidence a composition significantly different
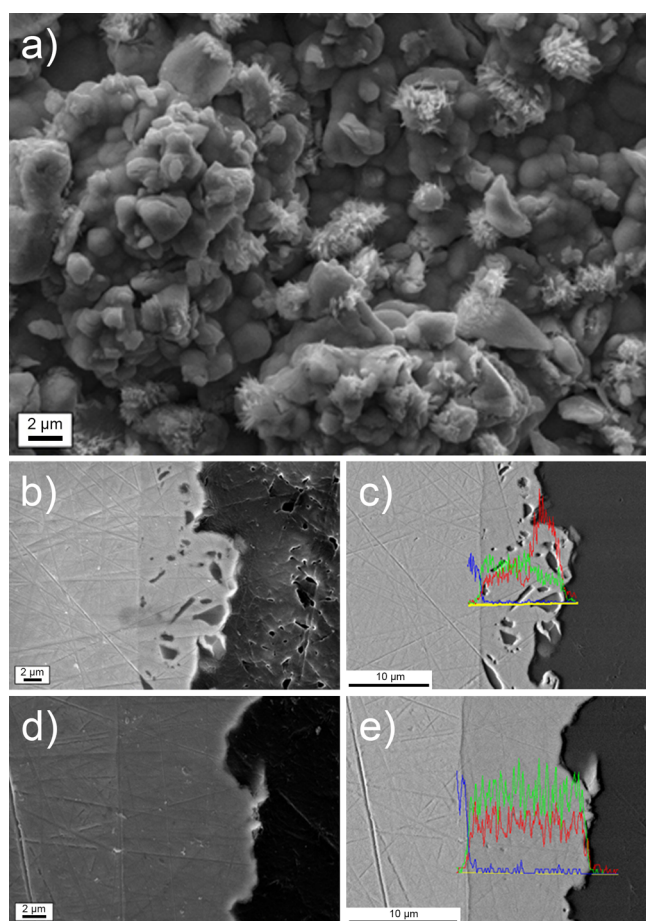
Figure 2. SEM image of the Ni−P/P codeposit after annealing (a); SEM cross section (b); and elemental line profile (c) of the Ni−P/P codeposit before annealing; SEM cross section (d) and elemental line profile (e) of the Ni−P/P codeposit after annealing at 400 °C for 1 h. In the two EDS line profiles, elements are represented by the following colors: red for P, green for Ni, and blue for Cu.

with respect to the surrounding zones of the sample. Different combinations of annealing time and temperature yielded similar morphologies, as visible in Figure S2 for a sample annealed at 400 °C for 1 h. The composition of the material after annealing was quantitatively assessed by mean of the EDS analysis (Table 1).

Table 1. Layer Composition before and after Annealing in Different Conditions

T ann. (°C)	T ann. (h)	P before ann. (% at.)	P after ann. (% at.)	P vapor pressure (mm Hg)
600	3	43	27.1	(molten)
400	2	43	29.4	480[50]
400	1	43	30.2	480[50]
300	1	43	31.4	21.5[50]

The main trend evidenced by the data reported in Table 1 is a progressive phosphorus depletion in the sample when the temperature or annealing time increases. This effect is a direct consequence of the relatively low melting point of red P, which implies a high vapor pressure that favors evaporation from the surface. For example, red P vapor pressure is 21.5 mm Hg at 300 °C and 480 mm Hg at 400 °C.[50] Also, prolonged annealing times favor P escape from the coating. At 300 °C

and for annealing times longer than 1 h, the P percentage was found to be lower than the minimum required to obtain a complete layer of stoichiometric Ni_2P (33.3% at.). Considering the reduced volume of the coating, it is evident that the total amount of evaporated P is very low. This allows optimal P usage, avoiding the presence of high initial amounts of elemental P in the oven.

In particular, a comparison can be done with respect to analogous phosphorization approaches that involve the use of red P. Normally, following these methodologies, a large excess of P is loaded in a reactor and evaporated. Unreacted P deposits on the walls of the reactor are actively removed by gas purging. For example, Wang et al.[38] and Mishra et al.[51] both used direct phosphorization from red P. Wang et al. used 500 mg of red P for each cm^2 of the treated substrate, while Mishra et al. used 100 mg per cm^2. In the case of our coatings, P content is nearly stoichiometric, implying an almost ideal usage of P during phosphorization. In detail, the mean weight per cm^2 of a 8 μm thick Ni−P/P layer was 4.85 mg/cm^2. Considering a P content of 43% at., the layer contained 1.38 mg/cm^2 of P. It is important to notice that this amount of P is present in the layer both as a component of the Ni−P solid solution and as elemental red P. After annealing, P content decreased from 43 to 31.4% at. (300 °C; 1 h). This variation implied a loss of P approximately equal to 0.16 mg/cm^2, which is orders of magnitude lower than the amounts lost by Wang et al. or Mishra et al.

Samples were cut and polished to observe their cross section after annealing. Coating thickness was measured from the cross-section images, resulting in a value of about 8 μm for a 90 min deposition time. Figure 2b depicts the Ni−P/P composite before annealing, while Figure 2d depicts the material after 1 h annealing at 400 °C. Red P particles are clearly evident in the first picture, while in the second one the cross section looks uniform. This constitutes a first evidence of the formation of a uniform phase after the reaction between Ni and P. EDS line profiles are acquired on the sample visible in Figure 2b, and the analysis revealed a significant P concentration discontinuity in correspondence of P particles (Figure 2c, red line). Coherently, P content is not zero in the matrix around the particles due to the presence of P in the form of a solid solution with Ni. If the same analysis is performed after annealing (Figure 2e), the result is significantly different. The concentration profile for the two elements, Ni and P, is roughly constant along the thickness of the layer, demonstrating once again the formation of a uniform material.

Phase composition of the materials obtained after annealing was determined via XRD. Ni−P solid solutions are in general amorphous above 9% wt P, while elemental P particles were found to be amorphous as well (Figure 1e). For these reasons, the Ni−P/P composite is expected to be amorphous too. This was confirmed by the XRD spectrum (Figure S5), where only Cu peaks from the substrate are visible.

After annealing, the formation of various phosphides was observed as a consequence of P interdiffusion and reaction with Ni. In particular, Ni_2P and $Ni_{12}P_5$ peaks were clearly detected. Ni_2P (JCPDS ref. code 00-013-0213) is characterized by a hexagonal crystal structure, exemplified in Figure S4. Its most relevant XRD peaks are located at 40.8° (111), 44.6° (201), 47.3° (210), 54.2° (300), 54.9° (211), 66.2° (310), 72.7° (311), 74.7° (400), and 80.9° (401). $Ni_{12}P_5$ (JCPDS ref. code 00-022-1190) has a tetragonal crystal lattice (Figure S3) and its most intense peaks are: 20.5° (200), 29° (211), 32.7°
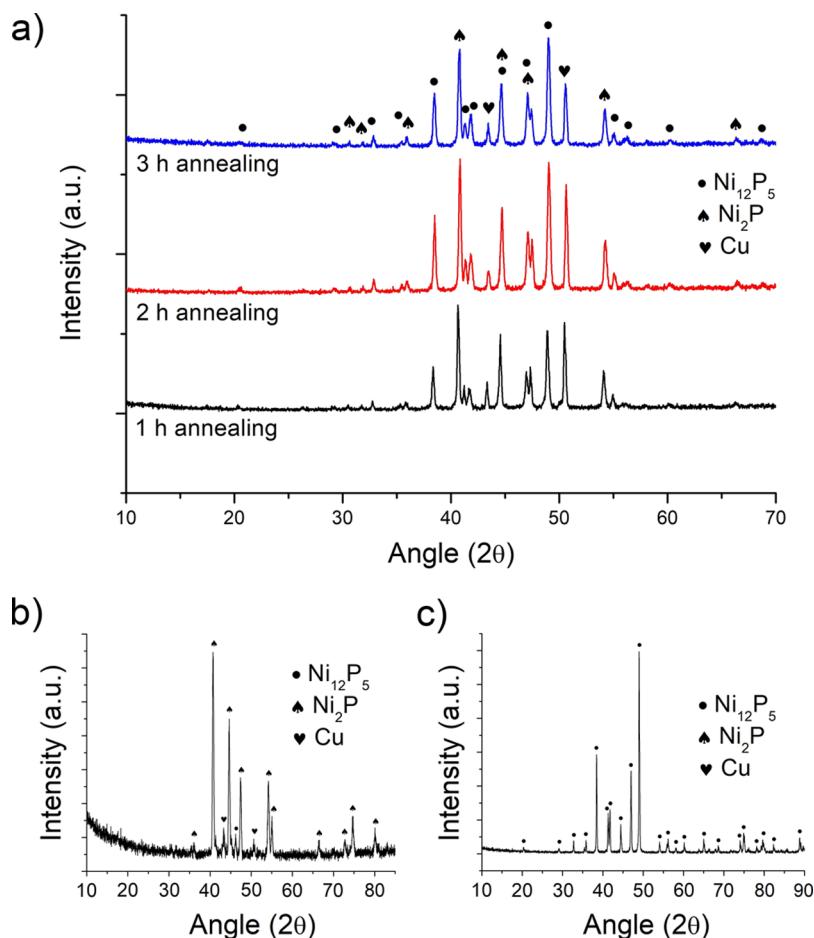
Figure 3. XRD of Ni−P/P annealed at 400 °C for increasing run times (a); XRD of Ni−P/P annealed at 300 °C for 1 h (b); and XRD of Ni−P/P annealed at 600 °C for 3 h (c).

(310), 38.4° (112), 41.6° (321), 41.7° (400), 44.4° (330), 47° (420), 49° (312), 56.2° (501), 60.1° (422), and 68.6° (620). To optimize Ni_2P formation, various annealing conditions were explored. In Figure 3a, the effect of annealing time was investigated by keeping constant the annealing temperature at 400 °C and varying the treatment time between 1 and 3 h. Conversely, the effect of annealing temperature was investigated by keeping constant the annealing time at 1 h and varying the annealing temperature. Figure 3b contains the data obtained at 300 °C, Figure 3a shows the data at 400 °C and Figure 3c depicts the behavior observed at 600 °C. In general, the annealing temperature and time had a great effect on the final phase composition of the electrocatalytic layer. At 400 °C, Ni_2P was found to coexist with $Ni_{12}P_5$ in all conditions. However, the annealing time was found to alter the relative ratio between the two phases. By comparing the relative height of the most intense peaks for $Ni_2P(111)$ and $Ni_{12}P_5(312)$, it was qualitatively noticed that higher annealing durations tend to enrich the final material with $Ni_{12}P_5$. The latter is the compound containing, in comparison with Ni_2P, less phosphorus. This phenomenon, which matches well with P depletion observed in Table 1, can be attributed to P evaporation from the surface. In particular, evaporation occurred simultaneously with phosphide precipitation inside the coating. Consequently, phosphides with less P formed.

The temperature was observed to have an effect even greater compared to annealing time. As stated, at 400 °C and 1 h annealing time, the phase composition of the coatings comprises both Ni_2P and $Ni_{12}P_5$. If annealing temperature is lowered to 300 °C, however, the phase composition of the layers dramatically changes, as evidenced in Figure 3b. In this condition, the layer contains mainly a pure Ni_2P phase, with a minor amount of $Ni_{12}P_5$. On the contrary, if the temperature is increased to 600 °C, the layer is characterized by the presence of the pure $Ni_{12}P_5$ phase. Once again, P evaporation from the layer was in competition with phosphide formation and thus actively controlled the phase composition of the final material.

The crystallite size of Ni_2P was estimated from the full-width-at-half-maximum (fwhm) of the most intense XRD peak using the Scherrer equation. For Ni_2P, the (111) reflection (40.8°) was considered. For $Ni_{12}P_5$, the (312) reflection was employed (49°). Samples annealed at 300 °C for 1 h were characterized by a crystallite size of 50 ± 6 nm (on the Ni_2P peak). Conversely, samples annealed at 400 °C for 2 h presented a crystallite size of 157 ± 22 nm (on the Ni_2P peak), while samples annealed at 600 °C for 3 h exhibited a crystallite size of 412 ± 38 nm (on the $Ni_{12}P_5$ peak). As expected, higher temperatures and longer annealing times induced a remarkable crystallite growth in the material.

According to XRD measurements, layers obtained after annealing at 300 °C for 1 h are composed almost entirely of Ni_2P. However, XRD is not able to give detailed information about the distribution of the phases inside the coating and the local composition of the surface. For this reason, XPS was
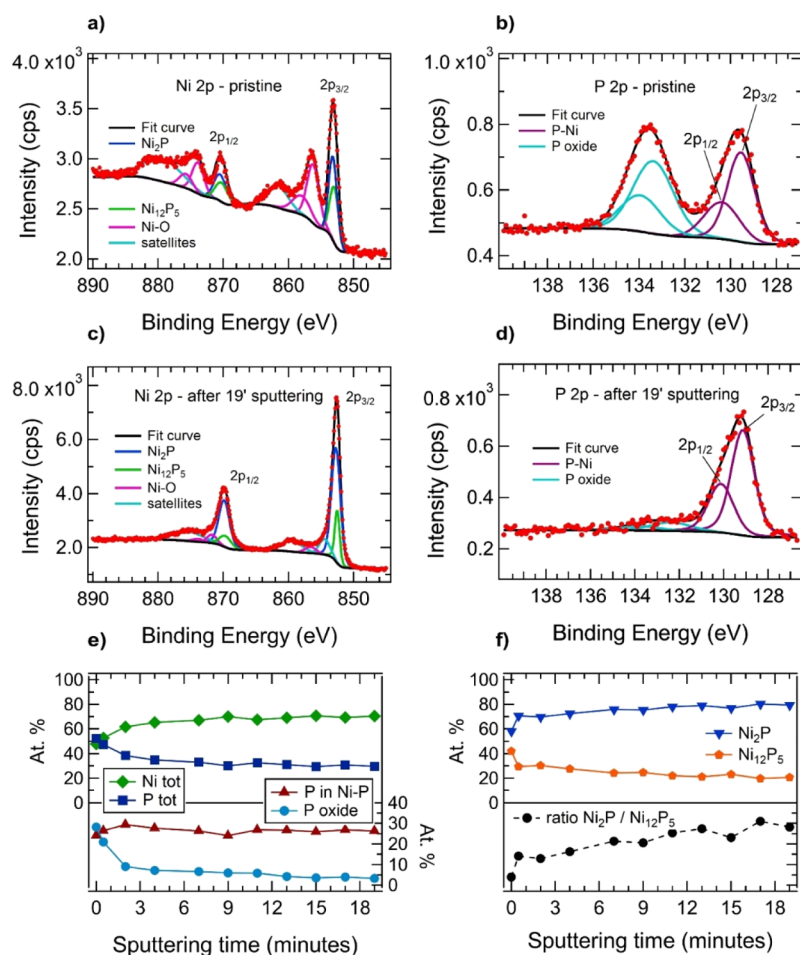
Figure 4. High-resolution XPS spectra in the Ni 2p region (a) and in the P 2p region (b) of the pristine sample; Ni 2p region (c) and P 2p region (d) of the sample after 19 min of sputtering; relative at. % of Ni and P (e, upper panel) and relative at. % of the P compound and oxide (e, lower panel) as a function of the sputtering time; relative at. % of Ni_2P and $Ni_{12}P_5$ (f, upper panel) and ratio of Ni_2P and $Ni_{12}P_5$ (f, lower panel) as a function of the sputtering time.

performed to determine the chemical state of the elements present in the first few nm close to the surface.

The XPS spectra were acquired on the sample annealed for 1 h at 300 °C. Depth profiling was carried out up to 19 min, that is, about 15 nm below the native surface. After the removal of the outmost layer, happening at around 4 min of sputtering, no further spectral evolution could be observed. The survey spectra up to 7 min are given in Figure S6. High-resolution XPS spectra of the Ni 2p region together with the peak fitting are shown in Figure 4a,c. The first figure exhibits the data acquired on the pristine sample, giving then information about the nontreated surface, the second one at the end of depth profiling corresponding to 19 min of sputtering. By looking at the data of the pristine sample, the Ni $2p_{3/2}$ peak at 853.2 eV, with a satellite at 861.3 eV, and Ni $2p_{1/2}$ peak at 870.4 eV, with a satellite at 879.9 eV, are assigned to nickel in the form of Ni–P phosphides.[52] Nickel oxide is probed by the $2p_{3/2}$ peak at 856.4 eV and the $2p_{1/2}$ peak at 873.8 eV. The satellites located at 6–8 eV above the main peaks contain overlapped contribution of phosphide and oxide species. Thus, these broad peaks were fitted with a single curve, whose fwhm's decreases as well as position shifts toward lower binding energies as a function of the sputtering time, reaching constant values after 4 min of sputtering (see Figure S7). These coexisting effects, namely, peak shrinking and energy shift,

could be associated to the loss of oxidized nickel present in the outermost layers, unveiling the predominance of Ni–P bonds in the bulk. The area ratio for the two spin orbit peaks $(2p_{1/2}:2p_{3/2})$ was imposed to be 0.5 either for the phosphide and for the oxide features. All the spectra of the pristine sample exhibit a shift of about 0.5 eV toward higher binding energy with respect to the sputtered sample (stabilized after 2 min of sputtering), that is, the peak is located at 852.7 eV (see Figure S7). Because the same shift is also present for the carbon peak (not shown), it indicates a moderate charging of the air-exposed surface of the specimen, which could be due to the presence of oxides, in particular to phosphorous bonded to oxygen (see below). The main Ni 2p feature was fitted with two distinct peaks, related to the contribution of $Ni_{12}P_5$ and Ni_2P, respectively.[53] Peak fitting was performed imposing the constrain of a 0.2 eV difference between the two peaks, as reported in the literature.[54] The quantitative analysis provides a trend of decrease of the $Ni_{12}P_5$ phase as a function of the sputtering time, as well as an increase of the Ni_2P phase. In figure 4f, which reports the ratio between Ni_2P and $Ni_{12}P_5$, shows a brutal rise during the first seconds of sputtering and then an almost linear increase. After the first 3 min of sputtering, the total amounts of either nickel and phosphorus are almost constant, indicating that no preferential sputtering in the alloy is observed (see Figure 4e, upper panel).
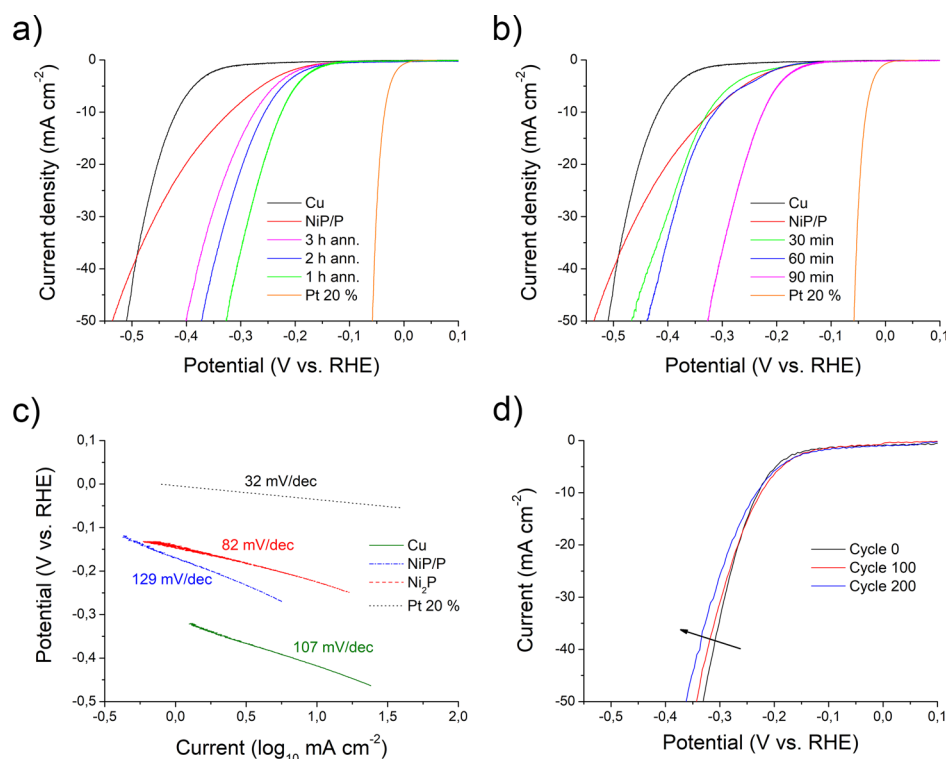
Figure 5. Electrocatalytic behavior of annealed Ni−P/P layers as a function of the annealing time (a); electrocatalytic behavior of annealed Ni−P/P layers as a function of catalyst loading (b); Tafel plots for annealed Ni−P/P (c); and cycling stability of the Ni−P/P layer annealed at 300 °C for 1 h (d).

Moreover, the abrupt decrease of the phosphorus oxide during the first sputtering minutes indicates that P is mainly oxidized in the outermost layers, even if a small and slightly decreasing P^{5+} survives also at the end of the sputtering procedure (Figure 4e, lower panel). The fact that a very small content of oxidized species is present, also once the surface layers have been removed, could be associated to a deep oxygen diffusion induced by thermal treatment. Table S1 reports the positions of the Ni $2p_{3/2}$, of the fitted peaks, and the distance between the Ni $2p_{3/2}$ and the satellite as a function of the sputtering time.

The high-resolution P 2p spectra were acquired at the same sputtering steps as Ni 2p, and Figure 4b,d shows the pristine sample and after 19 min of sputtering. Two main peaks are visible in the first spectrum: P in the Ni−P phosphides (129.6 eV) and P in the 5+ oxidation state (133.6 eV).[55] Because the P 2p peak has closely spaced spin−orbit components, namely, Δ = 0.9 eV, the spin−orbit splitting was imposed in the peak fitting together with an area ratio $(2p_{1/2}:2p_{3/2})$ of 0.5. Depth profiling highlights that the phosphorous oxide is mainly on the surface of the pristine sample and is suddenly removed by ion sputtering (see also Figure 4e, lower panel, and Figure S8). However, a residual amount of oxide remains in the bulk, again probably due to the thermally induced diffusion of oxygen inside the specimen. On the other hand, the restrained broadening of the peak centered at 129.4 eV could be related to phosphorous in various phosphide phases. This value of binding energy is about 0.3 eV lower with respect to elemental phosphorous, indicating a certain charge transfer typical of P in the form of phosphide. Nevertheless, the ratio trend, compared with the XRD results, reasonably leads to the assumption that both compounds are present in the material volume analyzed by XPS, which corresponds to few nm close to the surface.

3.4. Kinetic Considerations on Phosphide Formation.

The precipitation of Ni_2P and $Ni_{12}P_5$ in the layers subjected to annealing presents kinetic peculiarities that should be discussed, especially in light of the results obtained. Ni phosphide precipitation in electrodeposited Ni−P alloys is a well-known process.[56] In a normal high-P solid solution, however, precipitation takes place at appreciable rates only at relatively high temperatures (indicatively over 350 °C).[56−58] This consideration easily justifies the microstructure observed for the Ni−P/P layers annealed at 400 or 600 °C but not the phase composition observed at 300 °C. Such temperatures, applied for a comparatively short time of 1 h, should not allow the almost complete conversion to phosphide to occur. On the contrary, the material obtained in the present work shows a well-crystallized structure, with a very limited amorphous fraction. To explain this result, it can be guessed that a key contribution is given by the dispersion of elemental P in the Ni−P matrix. P is a highly reactive species in its elemental form, especially at high temperatures. When P diffuses in the Ni−P matrix, it may react with Ni accelerating phosphide formation. In addition, the P/Ni−P interface might provide preferential sites for the nucleation of phosphide particles. When Ni_2P forms in close proximity of a P particle, it may also accelerate P diffusion, considering that Ni_2P presents preferential diffusion of P along certain crystallographic planes.[59] Presently, the dominant mechanism cannot be identified and further studies are required. High vapor pressure of P constitutes a major challenge for phase optimization because it can promote P evaporation from the outer surface of the coating. Consequently, the P reaction and evaporation are reasonably in competition, with high temperatures and annealing times enhancing the latter. Obviously, the surface of the coating is a location of preferential evaporation, and this

consideration can probably explain its composition. As highlighted by XPS data, the surface presents a phase composition shifted toward $Ni_{12}P_5$ (which contains less P than Ni_2P).

3.5. HER Electrocatalytic Performances. After annealing, coatings were tested to assess their HER catalytic performances. Experiments were conducted in a 0.5 M H_2SO_4 solution, following the standard methodology present in most literature references for acidic HER testing. Effects of annealing time, temperature, and catalyst loading were investigated. Moreover, the catalytic behavior of the Cu substrate and of a 20% Pt commercial catalyst was assessed for comparison. The latter presented the behavior visible in Figure 5a, with a reference overpotential of 36 mV at 10 mA cm^{-2} (η_{10}). Cu is characterized by the behavior reported in Figure 5a, with a η_{10} of 418 mV.

Figure 5a describes the effect of annealing time on the electrocatalytic properties. Before annealing, samples presented a relatively poor electrocatalytic behavior (η_{10} of 320 mV; Figure 5a), which was dramatically enhanced by the permanence at high temperature for varying time lengths. Increasing annealing times decreased electrocatalytic performances, with η_{10} equal to 274 mV for 3 h, η_{10} equal to 256 mV for 2 h, and η_{10} equal to 224 mV for 1 h. The reason behind this performance is connected to the phase evolution evidenced by XRD and XPS. Longer annealing times favored the formation of $Ni_{12}P_5$, which has lower electrocatalytic properties, in place of Ni_2P. The samples annealed for 3 h are thus characterized by a $Ni_{12}P_5/Ni_2P$ ratio unbalanced toward $Ni_{12}P_5$, resulting in lower performances.

Figure 5b describes the effect of catalyst loading. In this case, catalyst loading can be assimilated to deposition time because the amount of the material deposited is directly dependent on deposition time. To calculate catalyst loading, the amount of Ni−P/P plated at each deposition time was estimated by the weight difference and divided by the area of the deposit. The following values were obtained: 1.78 mg cm^{-2} at 30 min of deposition, 3.61 mg cm^{-2} at 60 min, and 5.92 mg cm^{-2} at 90 min. As expected, catalyst loading increased roughly linearly with deposition time. By looking at Figure 5b, it appears evident that low deposition times present η_{10} values close to that obtained for nonannealed Ni−P/P (326 mV for 30 min and 313 mV for 60 min). Overpotential significantly dropped in the case of 90 min deposition (224 mV), indicating that a much more efficient catalytic layer was obtained. The reason for the behavior observed presumably resides in the evaporation behavior of P inside the coating. When deposition time is low, layer thickness is low as well. In this case, the volume of the coating is small, resulting in preferential P evaporation from the surface. Conversely, when the volume of the material is large, P can be supplied from the bulk to form phosphides with proper stoichiometry. In general, considering the results obtained, it appears evident that a higher residual phosphorus level in the layer can be connected to higher HER activity, as already evidenced in the literature.[29,60]

To evaluate catalysts kinetic properties, the acquired overpotential−current curves were replotted in the form of Tafel plots. As shown in Figure 5c, the Tafel slope for the Ni_2P containing layer (300 °C; 1 h) was 82 mV dec^{-1}, which is significantly lower than those of Ni−P/P (129 mV dec^{-1}) and Cu (107 mV dec^{-1}). These data suggest favorable HER kinetics, with an acceptable slope if compared to Pt (32 mV dec^{-1}). In particular, because of a decrease of 47 mV dec^{-1}, it

can be argued that HER is less limited by the Volmer reaction in the case of annealed Ni−P/P with respect to as-deposited Ni−P/P.[29] Consequently, hydrogen adsorbs on the surface of the phosphide layer with much faster kinetics.

Finally, performance stability of the material obtained in optimized conditions (300 °C; 1 h) was evaluated. Catalyst durability is critical to evaluate practical applicability of any catalyst, and good materials present relative stability for hundreds of cycles. Electrocatalytic layers obtained in the present work were cycled 200 times between 0 and −0.8 V versus Ag/AgCl at 50 mV s^{-1} and the resulting current−overpotential curves were acquired. A Ni_2P-containing catalyst showed good stability, as evidenced in Figure 5d. The overpotential difference $\Delta\eta_{10}$ between cycles 0 and 100 was limited to 5 mV, while the overpotential difference $\Delta\eta_{10}$ between cycles 0 and 200 was limited to 8 mV.

3.6. Comparison with State-of-the-Art Nickel Phosphide Electrocatalytic Layers. When compared with the current literature about hydrogen evolution from nickel phosphides in 0.5 M H_2SO_4, the layers described in the present work exhibit good electrocatalytic properties. The record observed overpotential to obtain a 10 mA cm^{-2} current was 224 mV versus RHE. It must be emphasized that the surface of the layers obtained in the present work is characterized by the coexistence of $Ni_{12}P_5$ and Ni_2P, as demonstrated by XPS. It is therefore not surprising that the record overpotential observed is more similar to the literature values typical of $Ni_{12}P_5$ rather than Ni_2P, despite the Ni_2P present in the bulk of the layers. For example, Pan et al.[61] report η_{10} values of 208 mV for $Ni_{12}P_5$ NPs and 137 mV for Ni_2P NPs obtained via thermal decomposition. Kucernak and Naranammalpuram Sundaram[29] report a η_{10} value of 208 mV for $Ni_{12}P_5$ NPs obtained from nickel(II) acetylacetonate and trioctylphosphine as precursors. Wang et al.[34] reported the production of Ni_2P-nanorods on Ni foam by means of direct red phosphorus solvothermal reaction. The value of η_{10} obtained in this case was 131 mV. In analogy with the present work, Zhang et al.[62] obtained mixed $Ni_{12}P_5−Ni_2P$ phosphides from thermally treated phosphonates. The recorded overpotential was, in that case, equal to 132 mV. Finally, if the comparison is extended to mixed metal phosphides, the electrocatalytic coatings obtained in the present work exhibit an overpotential larger than the values achieved with materials such as Co−Ni−P[63] or Fe−Ni−P[64] or others.[65−67] However, it is difficult to establish a comparison between different electrocatalytic systems because of the different forms of the phosphides employed. In fact, electrocatalytic efficiency depends strongly on the crystalline size in the case of bulk materials[68] and on dimension[69] and shape[70] in the case of NPs/nanorods.

4. CONCLUSIONS

Nickel phosphide electrocatalytic layers were produced employing a low-cost codeposition−annealing route. Elemental red phosphorus microparticles were successfully codeposited within a Ni−P matrix to overcome the intrinsic compositional limit of this electrochemical process. Phase control over the final phosphide composition was demonstrated by carefully selecting annealing conditions. Relatively low annealing times and temperatures, 1 h and 300 °C, respectively, were found to be optimal to form a phase pure Ni_2P phase. However, the surface of the phosphide layers was found to be depleted of phosphorus, resulting in a phase

composition containing significant amounts of $Ni_{12}P_5$. Such an altered superficial phase composition resulted in electrocatalytic performances intermediate between $Ni_{12}P_5$ and Ni_2P. A record overpotential of 224 mV versus RHE was observed at 10 mA cm^{-2} for layers annealed at 300 °C for 1 h, with favorable hydrogen evolution kinetics. Finally, good stability of the hydrogen evolution overpotential was observed, resulting in reproducible performances over time. The manufacturing methodology described in the present manuscript allows optimal phosphorus usage to be achieved because the material is directly codeposited in controlled amounts into the layer before annealing. This prevents excessive element waste and avoids the necessity of heating high quantities of phosphorus at high temperatures. In principle, the method here demonstrated can be applied to other transition metals that form a solid solution with phosphorus when electrodeposited, such as Fe−P or Co−P. Moreover, the metal matrix can be not only a solid solution but also a pure metal. This constitutes an attractive option for the production of metal phosphides such as CuP or MoP. All the cited phosphides present electrocatalytic properties, which makes them attractive alternatives for high cost Pt-based catalysts.

ASSOCIATED CONTENT

Supporting Information

The Supporting Information is available free of charge at https://pubs.acs.org/doi/10.1021/acsaem.0c00733.

> SEM image of an as deposited Ni−P layer; SEM picture of a Ni−P/P sample annealed at 400 °C for 1 h; Ni_2P and $Ni_{12}P_5$ crystallographic structures; XRD of as-deposited Ni−P/P; XPS survey spectra of annealed Ni−P/P for different sputtering times; XPS spectra and curve fitting of the Ni 2p region for different sputtering times; XPS spectra and curve fitting of the P 2p region for different sputtering times; and peak positions of a Ni $2p_{3/2}$ intermetallic peak, that is, centroid, $Ni_{12}P_5$ and Ni_2P, of the Ni−O peak, of satellite, and the distance between the centroid of the Ni $2p_{3/2}$ peak and the satellite as a function of the sputtering time (PDF)

AUTHOR INFORMATION

Corresponding Author

L. Magagnin − *Dipartimento di Chimica, Materiali e Ing. Chimica "Giulio Natta", Politecnico di Milano, 20131 Milano, Italy;* ⓞ orcid.org/0000-0001-5553-6441; Email: luca.magagnin@polimi.it

Authors

R. Bernasconi − *Dipartimento di Chimica, Materiali e Ing. Chimica "Giulio Natta", Politecnico di Milano, 20131 Milano, Italy;* ⓞ orcid.org/0000-0003-2193-8017

M. I. Khalil − *Dipartimento di Chimica, Materiali e Ing. Chimica "Giulio Natta", Politecnico di Milano, 20131 Milano, Italy*

C. Iaquinta − *C.I.Ma.I.Na., Dipartimento di Fisica "Aldo Pontremoli", Università di Milano, 20133 Milano, Italy*

C. Lenardi − *C.I.Ma.I.Na., Dipartimento di Fisica "Aldo Pontremoli", Università di Milano, 20133 Milano, Italy;* ⓞ orcid.org/0000-0002-5522-6803

L. Nobili − *Dipartimento di Chimica, Materiali e Ing. Chimica "Giulio Natta", Politecnico di Milano, 20131 Milano, Italy*

Complete contact information is available at:

https://pubs.acs.org/10.1021/acsaem.0c00733

Notes

The authors declare no competing financial interest.

REFERENCES

(1) Smalley, R. E. Future Global Energy Prosperity: The Terawatt Challenge. *MRS Bull.* **2005**, *30*, 412−417.

(2) Barton, J. P.; Infield, D. G. Energy Storage and Its Use with Intermittent Renewable Energy. *IEEE Trans. Energy Convers.* **2004**, *19*, 441−448.

(3) Goodenough, J. B. Electrochemical Energy Storage in a Sustainable Modern Society. *Energy Environ. Sci.* **2014**, *7*, 14−18.

(4) Vielstich, W.; Lamm, A.; Gasteiger, H. A. *Handbook of Fuel Cells: Fundamentals Technology and Applications*; Wiley: New York, 2003; Vol. 2.

(5) Gou, B.; Na, W.; Diong, B. *Fuel Cells: Modeling, Control, and Applications*; CRC Press, 2017.

(6) Souers, P. C. *Hydrogen Properties for Fusion Energy*; University of California Press, 1986.

(7) Züttel, A.; Remhof, A.; Borgschulte, A.; Friedrichs, O. Hydrogen: The Future Energy Carrier. *Philos. Trans. R. Soc., A* **2010**, *368*, 3329−3342.

(8) Mallouk, T. E. Divide and conquer. *Nat. Chem.* **2013**, *5*, 362−363.

(9) Ezaki, H.; Morinaga, M.; Watanabe, S. Hydrogen Overpotential for Transition Metals and Alloys, and Its Interpretation Using an Electronic Model. *Electrochim. Acta* **1993**, *38*, 557−564.

(10) Balbuena, P. B.; Subramanian, V. R. *Theory and Experiment in Electrocatalysis*; Springer, 2010.

(11) Santos, E.; Schmickler, W. *Catalysis in Electrochemistry: From Fundamental Aspects to Strategies for Fuel Cell Development*; John Wiley & Sons, 2011; Vol. 7.

(12) Kibler, L. A. Hydrogen Electrocatalysis. *ChemPhysChem* **2006**, *7*, 985−991.

(13) Mohammed-Ibrahim, J.; Sun, X. Recent progress on earth abundant electrocatalysts for hydrogen evolution reaction (HER) in alkaline medium to achieve efficient water splitting - A review. *J. Energy Chem.* **2019**, *34*, 111−160.

(14) Yuan, N.; Jiang, Q.; Li, J.; Tang, J. A Review on Non-Noble Metal Based Electrocatalysis for The Oxygen Evolution Reaction. *Arabian J. Chem.* **2020**, *13*, 4294−4309.

(15) Gong, M.; Wang, D.-Y.; Chen, C.-C.; Hwang, B.-J.; Dai, H. A Mini Review on Nickel-Based Electrocatalysts for Alkaline Hydrogen Evolution Reaction. *Nano Res.* **2016**, *9*, 28−46.

(16) Brown, D. E.; Mahmood, M. N.; Man, M. C. M.; Turner, A. K. Preparation and Characterization of Low Overvoltage Transition Metal Alloy Electrocatalysts for Hydrogen Evolution in Alkaline Solutions. *Electrochim. Acta* **1984**, *29*, 1551−1556.

(17) Safizadeh, F.; Ghali, E.; Houlachi, G. Electrocatalysis Developments for Hydrogen Evolution Reaction in Alkaline Solutions - A Review. *Int. J. Hydrogen Energy* **2015**, *40*, 256−274.

(18) Lv, H.; Xi, Z.; Chen, Z.; Guo, S.; Yu, Y.; Zhu, W.; Li, Q.; Zhang, X.; Pan, M.; Lu, G.; Mu, S.; Sun, S. A New Core/Shell NiAu/Au Nanoparticle Catalyst with Pt-like Activity for Hydrogen Evolution Reaction. *J. Am. Chem. Soc.* **2015**, *137*, 5859−5862.

(19) Faber, M. S.; Lukowski, M. A.; Ding, Q.; Kaiser, N. S.; Jin, S. Earth-Abundant Metal Pyrites (FeS_2, CoS_2, NiS_2, and Their Alloys) for Highly Efficient Hydrogen Evolution and Polysulfide Reduction Electrocatalysis. *J. Phys. Chem. C* **2014**, *118*, 21347−21356.

(20) Eftekhari, A. Electrocatalysts for hydrogen evolution reaction. *Int. J. Hydrogen Energy* **2017**, *42*, 11053−11077.

(21) Wang, F.; Li, Y.; Shifa, T. A.; Liu, K.; Wang, F.; Wang, Z.; Xu, P.; Wang, Q.; He, J. Selenium-Enriched Nickel Selenide Nanosheets as a Robust Electrocatalyst for Hydrogen Generation. *Angew. Chem., Int. Ed.* **2016**, *55*, 6919−6924.

(22) Xiao, P.; Chen, W.; Wang, X. A Review of Phosphide-Based Materials for Electrocatalytic Hydrogen Evolution. *Adv. Energy Mater.* **2015**, *5*, 1500985.

(23) Du, H.; Kong, R.-M.; Guo, X.; Qu, F.; Li, J. Recent Progress in Transition Metal Phosphides with Enhanced Electrocatalysis for Hydrogen Evolution. *Nanoscale* **2018**, *10*, 21617−21624.

(24) Wang, Y.; Kong, B.; Zhao, D.; Wang, H.; Selomulya, C. Strategies for Developing Transition Metal Phosphides as Heterogeneous Electrocatalysts for Water Splitting. *Nano Today* **2017**, *15*, 26−55.

(25) Yu, F.; Zhou, H.; Huang, Y.; Sun, J.; Qin, F.; Bao, J.; Goddard, W. A.; Chen, S.; Ren, Z. High-Performance Bifunctional Porous Non-Noble Metal Phosphide Catalyst for Overall Water Splitting. *Nat. Commun.* **2018**, *9*, 1−9.

(26) Chen, W.-F.; Muckerman, J. T.; Fujita, E. Recent Developments in Transition Metal Carbides and Nitrides as Hydrogen Evolution Electrocatalysts. *Chem. Commun.* **2013**, *49*, 8896−8909.

(27) Owens-Baird, B.; Kolen'ko, Y. V.; Kovnir, K. Structure-Activity Relationships for Pt-Free Metal Phosphide Hydrogen Evolution Electrocatalysts. *Chem.—Eur J.* **2018**, *24*, 7298−7311.

(28) Huang, Z.; Chen, Z.; Chen, Z.; Lv, C.; Meng, H.; Zhang, C. Ni12P5 Nanoparticles as an Efficient Catalyst for Hydrogen Generation via Electrolysis and Photoelectrolysis. *ACS Nano* **2014**, *8*, 8121−8129.

(29) Kucernak, A. R. J.; Naranammalpuram Sundaram, V. N. Nickel Phosphide: The Effect of Phosphorus Content on Hydrogen Evolution Activity and Corrosion Resistance in Acidic Medium. *J. Mater. Chem. A* **2014**, *2*, 17435−17445.

(30) Wexler, R. B.; Martirez, J. M. P.; Rappe, A. M. Active Role of Phosphorus in the Hydrogen Evolving Activity of Nickel Phosphide (0001) Surfaces. *ACS Catal.* **2017**, *7*, 7718−7725.

(31) Park, J.; Koo, B.; Yoon, K. Y.; Hwang, Y.; Kang, M.; Park, J.-G.; Hyeon, T. Generalized Synthesis of Metal Phosphide Nanorods via Thermal Decomposition of Continuously Delivered Metal−Phosphine Complexes Using a Syringe Pump. *J. Am. Chem. Soc.* **2005**, *127*, 8433−8440.

(32) Read, C. G.; Callejas, J. F.; Holder, C. F.; Schaak, R. E. General Strategy for the Synthesis of Transition Metal Phosphide Films for Electrocatalytic Hydrogen and Oxygen Evolution. *ACS Appl. Mater. Interfaces* **2016**, *8*, 12798−12803.

(33) Liu, Z.; Huang, X.; Zhu, Z.; Dai, J. A Simple Mild Hydrothermal Route for the Synthesis of Nickel Phosphide Powders. *Ceram. Int.* **2010**, *36*, 1155−1158.

(34) Wang, X.; Kolen'ko, Y. V.; Liu, L. Direct Solvothermal Phosphorization of Nickel Foam to Fabricate Integrated Ni2P-Nanorods/Ni Electrodes for Efficient Electrocatalytic Hydrogen Evolution. *Chem. Commun.* **2015**, *51*, 6738−6741.

(35) Zhang, G.; Xu, Q.; Liu, Y.; Qin, Q.; Zhang, J.; Qi, K.; Chen, J.; Wang, Z.; Zheng, K.; Swierczek, K.; Zheng, W. Red Phosphorus as Self-Template to Hierarchical Nanoporous Nickel Phosphides toward Enhanced Electrocatalytic Activity for Oxygen Evolution Reaction. *Electrochim. Acta* **2020**, *332*, 135500.

(36) Xiao, J.; Lv, Q.; Zhang, Y.; Zhang, Z.; Wang, S. One-Step Synthesis of Nickel Phosphide Nanowire Array Supported on Nickel Foam with Enhanced Electrocatalytic Water Splitting Performance. *RSC Adv.* **2016**, *6*, 107859−107864.

(37) Wang, X.; Kolen'ko, Y. V.; Bao, X.-Q.; Kovnir, K.; Liu, L. One-Step Synthesis of Self-Supported Nickel Phosphide Nanosheet Array Cathodes for Efficient Electrocatalytic Hydrogen Generation. *Angew. Chem., Int. Ed.* **2015**, *54*, 8188−8192.

(38) Wang, X.; Li, W.; Xiong, D.; Petrovykh, D. Y.; Liu, L. Bifunctional Nickel Phosphide Nanocatalysts Supported on Carbon Fiber Paper for Highly Efficient and Stable Overall Water Splitting. *Adv. Funct. Mater.* **2016**, *26*, 4067−4077.

(39) Wang, X.; Li, W.; Xiong, D.; Liu, L. Fast Fabrication of Self-Supported Porous Nickel Phosphide Foam for Efficient, Durable Oxygen Evolution and Overall Water Splitting. *J. Mater. Chem. A* **2016**, *4*, 5639−5646.

(40) Xing, J.; Zou, Z.; Guo, K.; Xu, C. The Effect of Phosphating Time on the Electrocatalytic Activity of Nickel Phosphide Nanorod Arrays Grown on Ni Foam. *J. Mater. Res.* **2018**, *33*, 556−567.

(41) Nath, N. S.; Bhattacharya, I.; Tuck, A. G.; Schlipalius, D. I.; Ebert, P. R. Mechanisms of Phosphine Toxicity. *J. Toxicol.* **2011**, *2011*, 1−9.

(42) Sparling, D. W.; Day, D.; Klein, P. Acute Toxicity and Sublethal Effects of White Phosphorus in Mute Swans, Cygnus Olor. *Arch. Environ. Contam. Toxicol.* **1999**, *36*, 316−322.

(43) Brodkin, J. Preparation of White Phosphorus from Red Phosphorus. *J. Chem. Educ.* **1960**, *37*, A93.

(44) Lelevic, A.; Walsh, F. C. Electrodeposition of Ni P alloy coatings: A review. *Surf. Coating. Technol.* **2019**, *369*, 198−220.

(45) Alleg, S.; Boussaha, A.; Tebib, W.; Zergoug, M.; Suňol, J. J. Microstructure and Magnetic Properties of Nip Alloys. *J. Supercond. Nov. Magnetism* **2016**, *29*, 1001−1011.

(46) Bonino, J.-P.; Bruet-Hotellaz, S.; Bories, C.; Pouderoux, P.; Rousset, A. Thermal Stability of Electrodeposited Ni−P Alloys. *J. Appl. Electrochem.* **1997**, *27*, 1193−1197.

(47) Graydon, J. W.; Kirk, D. W. Suspension Electrodeposition of Phosphorus and Copper. *J. Electrochem. Soc.* **1990**, *137*, 2061−2066.

(48) Schurecht, H. G. Sedimentation as a Means of Classifying Extremely Fine Clay Particles1. *J. Am. Ceram. Soc.* **1921**, *4*, 812−821.

(49) Okamoto, H. Ni-P (Nickel-Phosphorus). *J. Phase Equilibria Diffus.* **2010**, *31*, 200−201.

(50) Melville, H. W.; Gray, S. C. The Vapour Pressure of Red Phosphorus. *Trans. Faraday Soc.* **1936**, *32*, 1026−1030.

(51) Mishra, I. K.; Zhou, H.; Sun, J.; Dahal, K.; Ren, Z.; He, R.; Chen, S.; Ren, Z. Highly Efficient Hydrogen Evolution by Self-Standing Nickel Phosphide-Based Hybrid Nanosheet Arrays Electrocatalyst. *Mater. Today Phys.* **2018**, *4*, 1−6.

(52) Chen, G.-F.; Ma, T. Y.; Liu, Z.-Q.; Li, N.; Su, Y.-Z.; Davey, K.; Qiao, S.-Z. Efficient and Stable Bifunctional Electrocatalysts Ni/Ni x M y (M = P, S) for Overall Water Splitting. *Adv. Funct. Mater.* **2016**, *26*, 3314−3323.

(53) Xin, H.; Guo, K.; Li, D.; Yang, H.; Hu, C. Production of High-Grade Diesel from Palmitic Acid over Activated Carbon-Supported Nickel Phosphide Catalysts. *Appl. Catal. B Environ.* **2016**, *187*, 375−385.

(54) Elsener, B.; Atzei, D.; Krolikowski, A.; Rossi, A. Effect of Phosphorus Concentration on the Electronic Structure of Nanocrystalline Electrodeposited Ni-P Alloys: An XPS and XAES Investigation. *Surf. Interface Anal.* **2008**, *40*, 919−926.

(55) Sun, T.; Dong, J.; Huang, Y.; Ran, W.; Chen, J.; Xu, L. Highly active and stable electrocatalyst of Ni2P nanoparticles supported on 3D ordered macro-/mesoporous Co-N-doped carbon for acidic hydrogen evolution reaction. *J. Mater. Chem. A* **2018**, *6*, 12751−12758.

(56) Guo, Z.; Keong, K. G.; Sha, W. Crystallisation and Phase Transformation Behaviour of Electroless Nickel Phosphorus Platings during Continuous Heating. *J. Alloys Compd.* **2003**, *358*, 112−119.

(57) Jiaqiang, G.; Yating, W.; Lei, L.; Bin, S.; Wenbin, H. Crystallization Temperature of Amorphous Electroless Nickel-Phosphorus Alloys. *Mater. Lett.* **2005**, *59*, 1665−1669.

(58) Calvo-Dahlborg, M.; Machizaud, F.; Nhien, S.; Vigneron, B.; Dahlborg, U. Structural Study of a Phase Transition in a NiP Metallic Glass. *Mater. Sci. Eng., A* **1997**, *226−228*, 197−203.

(59) Contreras-Mora, J.; Ariga-Miwa, H.; Takakusagi, S.; Williams, C. T.; Asakura, K. Phosphorous Diffusion Through Ni2P-Low Energy Diffusion Path and Its Unique Local Structure. *J. Phys. Chem. C* **2018**, *122*, 6318−6322.

(60) Menezes, P. W.; Indra, A.; Das, C.; Walter, C.; Göbel, C.; Gutkin, V.; Schmeiβer, D.; Driess, M. Uncovering the Nature of Active Species of Nickel Phosphide Catalysts in High-Performance Electrochemical Overall Water Splitting. *ACS Catal.* **2017**, *7*, 103−109.

(61) Pan, Y.; Liu, Y.; Zhao, J.; Yang, K.; Liang, J.; Liu, D.; Hu, W.; Liu, D.; Liu, Y.; Liu, C. Monodispersed Nickel Phosphide Nanocrystals with Different Phases: Synthesis, Characterization and

Electrocatalytic Properties for Hydrogen Evolution. *J. Mater. Chem. A* **2015**, *3*, 1656−1665.

(62) Zhang, R.; Russo, P. A.; Feist, M.; Amsalem, P.; Koch, N.; Pinna, N. Synthesis of Nickel Phosphide Electrocatalysts from Hybrid Metal Phosphonates. *ACS Appl. Mater. Interfaces* **2017**, *9*, 14013−14022.

(63) Liu, J.; Wang, Z.; David, J.; Llorca, J.; Li, J.; Yu, X.; Shavel, A.; Arbiol, J.; Meyns, M.; Cabot, A. Colloidal Ni2−xCoxP nanocrystals for the hydrogen evolution reaction. *J. Mater. Chem. A* **2018**, *6*, 11453−11462.

(64) Ma, Z.; Li, R.; Wang, M.; Meng, H.; Zhang, F.; Bao, X.-Q.; Tang, B.; Wang, X. Self-Supported Porous Ni-Fe-P Composite as an Efficient Electrocatalyst for Hydrogen Evolution Reaction in Both Acidic and Alkaline Medium. *Electrochim. Acta* **2016**, *219*, 194−203.

(65) Yuan, H.; Wang, S.; Gu, X.; Tang, B.; Li, J.; Wang, X. One-Step Solid-Phase Boronation to Fabricate Self-Supported Porous FeNiB/FeNi Foam for Efficient Electrocatalytic Oxygen Evolution and Overall Water Splitting. *J. Mater. Chem. A* **2019**, *7*, 19554−19564.

(66) Zhang, W.; Zheng, J.; Gu, X.; Tang, B.; Li, J.; Wang, X. Facile synthesis, characterization and DFT studies of a nanostructured nickel-molybdenum-phosphorous planar electrode as an active electrocatalyst for the hydrogen evolution reaction. *Nanoscale* **2019**, *11*, 9353−9361.

(67) Jiang, N.; You, B.; Sheng, M.; Sun, Y. Electrodeposited Cobalt-Phosphorous-Derived Films as Competent Bifunctional Catalysts for Overall Water Splitting. *Angew. Chem., Int. Ed.* **2015**, *54*, 6251−6254.

(68) Markovic, N.; Gasteiger, H.; Ross, P. N. Kinetics of Oxygen Reduction on Pt(hkl) Electrodes: Implications for the Crystallite Size Effect with Supported Pt Electrocatalysts. *J. Electrochem. Soc.* **1997**, *144*, 1591−1597.

(69) Hayden, B. E. Particle Size and Support Effects in Electrocatalysis. *Acc. Chem. Res.* **2013**, *46*, 1858−1866.

(70) Seo, B.; Baek, D. S.; Sa, Y. J.; Joo, S. H. Shape Effects of Nickel Phosphide Nanocrystals on Hydrogen Evolution Reaction. *CrystEngComm* **2016**, *18*, 6083−6089.